

Article

Temperature Drift Compensation for High-G MEMS Accelerometer Based on RBF NN Improved Method

Min Zhu ^{1,2,†}, Lixin Pang ³, Zhijun Xiao ¹, Chong Shen ^{1,†} , Huiliang Cao ^{1,*} , Yunbo Shi ¹
and Jun Liu ^{1,*}

¹ Science and Technology on Electronic Test & Measurement Laboratory, North University of China, Tai Yuan 030051, China; 1607024104@st.nuc.edu.cn (M.Z.); 1506014442@st.nuc.edu.cn (Z.X.); shenchong@nuc.edu.cn (C.S.); shiyunbo@nuc.edu.cn (Y.S.)

² School of Electrical and Control Engineering, North University of China, Tai Yuan 030051, China

³ APT Mobile Satcom Limited, Shenzhen 518126, China; plx@apsatcom.com

* Correspondence: caohuiliang1986@126.com (H.C.); liuj@nuc.edu.cn (J.L.);
Tel.: +86-186-3696-1516 (H.C. & J.L.)

† The two authors have the equal contribution to this work.

Received: 5 January 2019; Accepted: 14 February 2019; Published: 18 February 2019



Abstract: In this paper, the method for compensating the temperature drift of high-G MEMS accelerometer (HGMA) is proposed, including radial basis function neural network (RBF NN), RBF NN based on genetic algorithm (GA), RBF NN based on GA with Kalman filter (KF), and the RBF NN + GA + KF method compensated by the temperature drift model. First, this paper introduces an HGMA structure working principle, conducts a finite element analysis, and produces the results. The simulation results show that the HGMA working mode is the 1st order mode, and its resonant frequency is 408 kHz. The 2nd order mode resonant frequency is 667 kHz, and the gap with the first mode is 260 kHz, indicating that the coupling movement between the two modes is tiny, so the HGMA has good linearity. Then, a temperature experiment is performed to obtain the output value of HGMA. The output values of HGMA are analyzed and optimized by using the algorithms proposed in this paper. The processing results show that the RBF NN + GA + KF method compensated by the temperature drift model achieves the best denoising consequent. The processing results show that the temperature drift of the HGMA is effectively compensated. The final results show that acceleration random walking improved from 17130 g/h/Hz^{0.5} to 765.3 g/h/Hz^{0.5}, and bias stability improved from 4720 g/h to 57.27 g/h, respectively. The results show that after using the RBF NN + GA + KF method, combined with the temperature drift model, the temperature drift trend and noise characteristics of HGMA are well optimized.

Keywords: high-G MEMS accelerometer; theoretical simulation; temperature drift compensation; radial basis function neural network; genetic algorithm; Kalman Filter

1. Introduction

A high-range, impact-resistant, high-G micro electro mechanical system (MEMS) accelerometer (HGMA) has important applications in navigation, defense, and impact measurement [1]. Temperature is the main reason for limiting the accuracy of a high-G MEMS accelerometer. A large body of research has been dedicated to improving the temperature characteristics of a high-G MEMS accelerometer. In general, there are two main methods for temperature compensation: hardware compensation methods, and software compensation methods.

The hardware methods include optimizing the MEMS accelerometer structure or controlling the MEMS accelerometer operating temperature. For example: Liu proposed a high-precision capacitive

MEMS accelerometer temperature compensation method, which is based on parasitic resistance [2]. Li designed a new differential silicon substrate, which can significantly reduce the temperature drift of the accelerometer [3]. Tsai developed a complementary metal-oxide-semiconductor (CMOS) micro-electromechanical system (MEMS) accelerometer. The accelerometer has higher sensitivity and suppresses temperature drift significantly [4]. Xu proposed an INS/uwb integrated system based on uwb to effectively reduce the drift error of the sensor [5]. Yang proposed that architecture use an on-chip temperature sensor to achieve on-chip temperature compensation, and a micro-heater to realize on-chip temperature control of the sensor [6]. Cao analyzed the noise and temperature compensation method of the MEMS gyroscope and studied the circuit interface structure and bandwidth of the MEMS sensor, effectively suppressing the noise of the MEMS sensor [7–10]. To a certain extent, the hardware compensation method does not only increase the volume and power consumption of the accelerometer, but also increases costs, so the hardware method is not applicable in applications that require low cost and low power consumption.

The second compensation method is the software method, which studies the law between the temperature and the output signal of the MEMS accelerometer, and then establishes a temperature drift model to compensate the effects of temperature drift. For example: Lee proposed that the impact of temperature changes on accelerometers can be reduced by accurately predicting and compensating for the temperature sensitivity of resonant frequency [11]. Li studied the static temperature mathematic model of quartz flexible accelerometer to then obtain temperature compensation of the accelerometer by DSP operation [12]. Dominik combines the experimental method with the numerical simulation method to provide ceramic acceleration with good accuracy in high temperature environments [13]. Yang proposed a new, simple mathematical model that makes the sensor output more robust at high temperatures, which was successfully applied to two low-cost quartz accelerometers [14]. He established an analytical model for the temperature drift of bias (TDB) and temperature drift of scale factor (TDSF), which is based on the analysis results of thermal deformation and stiffness temperature dependence. This model can effectively improve the accuracy of a silicon MEMS capacitive accelerometer [15]. Cao proposed to use multiple fading factors for a strong tracking Kalman filter (STKF), which can better adapt to the uncertainty of the accelerometer error model [16]. Ruzza obtained original data through the temperature test and established a low-order polynomial equation, combined it with the measurement error caused by thermal drift, and then used them in the temperature drift compensation of the accelerometer [17]. Shen proposed a parallel processing algorithm of the temperature error based on variational mode decomposition (VMD) and an augmented nonlinear differentiator (AND), which can increase the efficiency of temperature error processing [18]. Zhang proposed a complete analytical model based on the Hamilton's principle, which provides a new perspective for studying the relationship between temperature and nonlinearity [19]. Cheng proposed a modification of an radial basis function neural network (RBF ANN) based on temperature compensation models for interferometric fiber optical gyroscopes (IFOGs) [20]. Huang proposed that the appropriate filter be designed according to different error models; they then combined the multi-model method with the extended Kalman filter (EKF) method to estimate the state optimally, which improves the accuracy and effectiveness of the sensor [21]. Xu proposed a federated extended finite impulse response (EFIR) filter to improve the accuracy of the sensor [22]. Shen proposed a new multi-input/single-output model based on genetic algorithm (GA) and Elman neural network (Elman NN) to improve the temperature drift modeling accuracy of the sensor [23]. Xia proposed a temperature prediction and control model based on BP NN and Fuzzy-PID control method, which can successfully reduce the zero-rate output [24]. Software methods offer advantages of simple structure, low cost and convenient implementation, and are convenient for improving the precision of the MEMS accelerometer.

RBF NN based on GA has been proposed and successfully applied to the temperature drift model of the MEMS gyroscope [25]. Unlike previous accelerometer temperature drift models, a new fusion algorithm (RBF + NN + GA + KF combined with temperature drift model) was proposed in this paper

to make the accelerometer more accurate. The new algorithm considers not only temperature and temperature variation rate, but also temperature product term.

The paper will be introduced as follows: The structure of the MEMS accelerometer and the temperature experiment are described in Section 2; the temperature drift model and fusion algorithm are shown in Section 3; Section 4 shows the temperature experiment; and Section 5 shows the results of data processing and the analysis results of various algorithms. The conclusions are given in Section 6.

2. Structure of MEMS Accelerometer and Temperature Experiment

Work Mode Analysis

The original signal collected in this paper is from a newly designed and manufactured high-G MEMS accelerometer (HGMA) [26,27]. It has a high impact survival rate and high measuring range. The detection method of the HGMA is piezoresistance, and output signal is voltage. HGMA adopts four beams and an island structure. The frame, four beams and center mass are all rectangular, which is conducive to processing. Its structure diagram and parameters are shown in Figure 1.

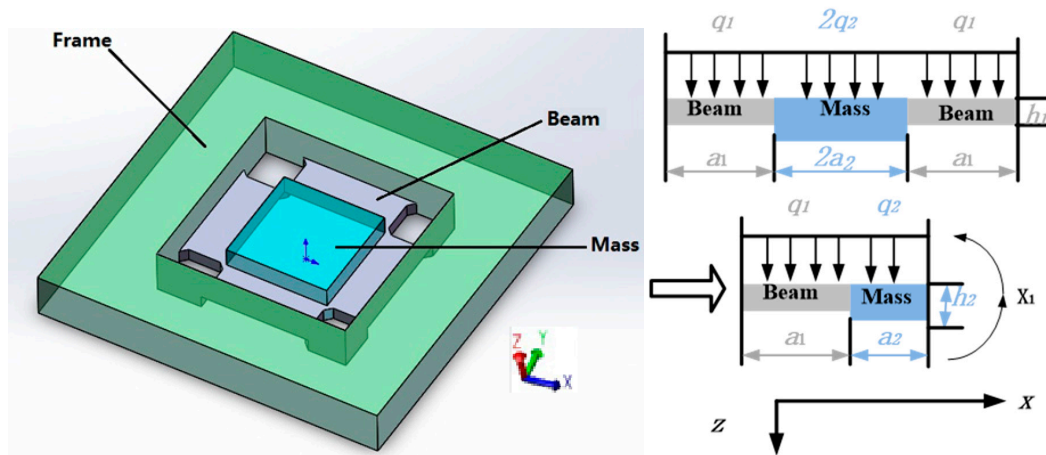


Figure 1. HGMA structure schematic and size.

The coordinate system is constructed with the cross section of the accelerometer. The central dividing line of the cross section is the Z axis (the direction is positive when downward). The other middle line is the X axis, and the right direction is positive. The frame constructed is shown in Figure 1. The beam’s length, width and thickness are a_1 , b_1 and c_1 , respectively, and the mass’s length, width and thickness are $2a_2$, b_2 and c_2 , respectively. The size values are shown in Table 1.

Table 1. Structural parameters of the HGMA.

	Beam			Mass		
Parameters	length (a_1)	width (b_1)	height (c_1)	length (a_2)	width (b_2)	height (c_1)
Size/ μm	350	800	80	800	800	200

The accelerometer structure mode distribution is simulated and analyzed through ANSYS soft at four primary resonance modes, and shown in Figure 2a–d as the first, second, third and fourth modes, respectively. The first mode mass moves along the Z axis, and is the working mode. The second mode mass rotates around the X-axis. The third mode mass rotates around the Y-axis. The fourth mode mass and frame move along the Z axis. The resonant frequencies of the four modes are shown in Table 2, which indicates that the 1st order is the working mode of HGMA and its resonant frequency is 408 kHz. The 2nd order mode resonant frequency is 667 kHz and has 260 kHz gap with the 1st mode, which means that the coupling movement between these two modes is tiny and good for HGMA linearity.

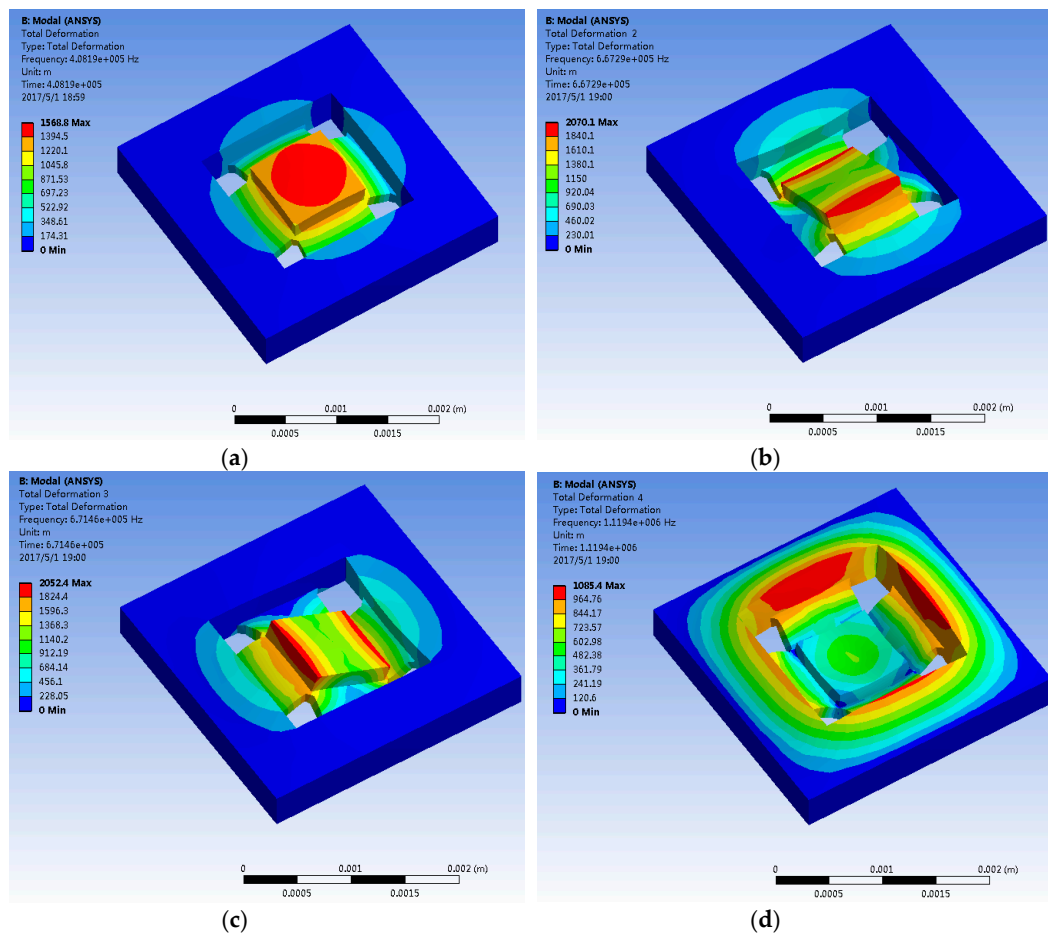


Figure 2. Mode simulation of HGMA structure: (a) (b) (c) and (d) are 1st, 2nd, 3rd and 4th order modes.

Table 2. Resonant frequencies of the four modes.

Mode Shapes	1	2	3	4
Resonant Frequency /kHz	408	667	671	1119

The structure of HGMA is made of silicon and bonding on glass. The main technological process is mainly divided into 12 steps. The SEM photos and CCD photos of the accelerometer structure are shown in Figure 3.

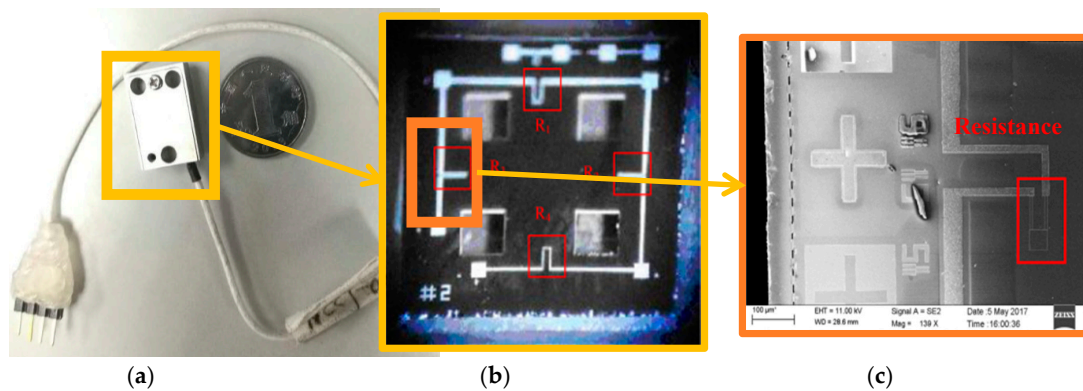


Figure 3. (a) HGMA overall photo; (b) CCD photo; (c) SEM photo of HGMA.

3. Model and Algorithm

3.1. Temperature Drift Model

In this paper, in order to solve the temperature drift problem of HGMA mentioned in Section 2, a new MEMS temperature drift model is established. Three factors (temperature, temperature variation rate and temperature product term) are considered in this model. They can fully reflect the temperature condition of the MEMS accelerometer. Therefore, it is beneficial to improve the accuracy of the accelerometer. The three-factor matrix C is shown in Equation (1).

$$C = \begin{bmatrix} T \\ \dot{T} \\ T \times \Delta T \end{bmatrix} \tag{1}$$

where T is the temperature, \dot{T} is the rate of temperature variation rate, and $T \times \Delta T$ is the product term. Then, the complex model is constructed by a neural network, and these three factors are used as inputs to the model, just as shown in Figure 4. Let $F(\cdot)$ be the objective function to be trained. The objective function is shown in Equation (2):

$$E = F(C) = F\left\{ \begin{bmatrix} T \\ \dot{T} \\ T \times \Delta T \end{bmatrix} \right\} \tag{2}$$

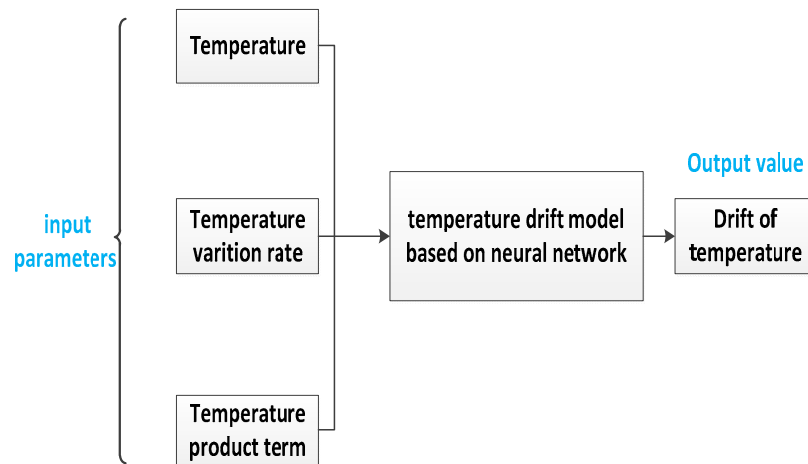


Figure 4. The framework of the temperature drift model.

3.2. The Algorithm of RBF NN

RBF is a non-negative and non-linear function with local distribution of center points and symmetric attenuation of radial center points. The local distribution of center point means that when the input is in a specified small area, the RBF of the hidden unit will achieve a meaningful non-zero response. Radial symmetric attenuation means that the response of RFB depends on the input point closer to the center of the RBF. The closer the input point is to the center of RBF, the more sensitive the output variable is, and the stronger the generated output signal can be.

A hidden layer of neural work is introduced into the RBF, and then RBF NN is established. RBF NN has a similar neural network structure as other forward neural networks. The RBF neural network has only three layers, and each layer structure has its own unique characteristics. As shown in Figure 5, it has a perceptual-associative-response structure. Compared with other neural networks, RFB neural network has advantages of strong classification ability, simple optimization process, and

fast learning speed. When the RBF NN has more hidden layer neuron nodes, it has a stronger computing ability, mapping ability, and better function approximation ability, so it can approach a complex function curve with arbitrary precision [20].

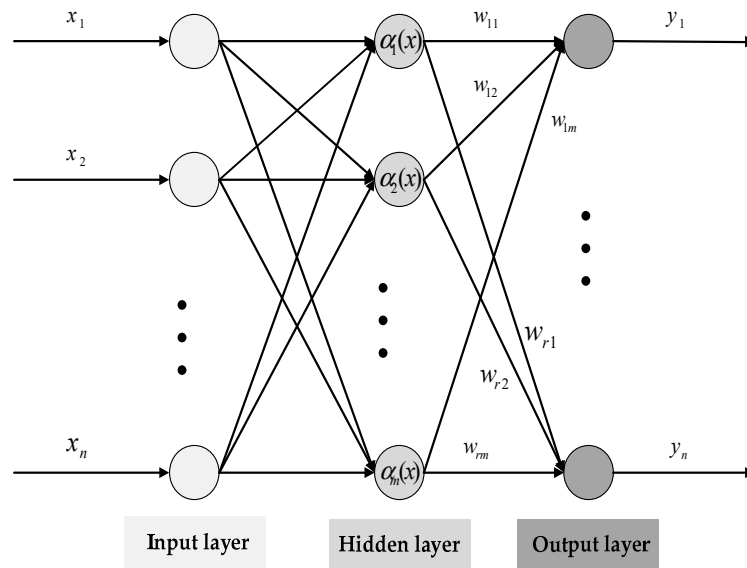


Figure 5. Model of radial basis function neural network.

The basis function of RBF NN is shown in Equation (3).

$$\alpha_j(x) = \psi_j(\|x - c_j\|/\sigma_j) \tag{3}$$

where $\alpha_j(x)$ is a radial basis function, $\| \cdot \|$ is an exemplary number, usually taken as the Euclidean norm, c_j is the center point of the function in j , σ_j is the breadth of the hidden layer neuron around the basis function, $\|x - c_j\|$ is the Euclidean distance from x to c_j , ψ_j has a maximum value at c_j , which is a radially symmetric function. When $\|x - c_j\|$ increases, ψ_j decreases to zero quickly. For the determined value of x , only a few processing elements that is near the center can be activated.

Generally, there are three types of radial basis functions: Gaussian functions, multiple quadratic functions, and wavelet functions. Gaussian functions are the most commonly used, shown in Equation (4).

$$\alpha_j(x) = \psi_j(\|x - c_j\|/\sigma_j) = e^{-\frac{\|x - c_j\|^2}{2\sigma_j^2}} \tag{4}$$

The network output of the RBF NN is shown in Equation (5).

$$y = W\alpha(x) \text{ or } y_i = \sum_{j=1}^m w_{ij}\alpha_j(x), i = 1, 2, \dots, r \tag{5}$$

where w_{ij} is the connection weight between the i -th hidden layer node and the j -th output layer node.

The learning algorithm with weights is shown in Equation (6).

$$w_{ij}(l + 1) = w_{ij}(l) + \beta[y_i^d - y_i(l)]\alpha_j(x)/\alpha^T(x)\alpha(x) \tag{6}$$

where β is the learning rate. In order to improve the convergence performance of the iterative learning algorithm, the range of β is 0 to 2.

During the training process of the algorithm NN, when x is far away from c_j , the output of $\alpha_j(x)$ is also nearly close to 0 when passing through the linear nerve of the second layer. The value of the corresponding weight will also be affected, if the value of $\alpha_j(x)$ is more than a value such as 0.06.

When x and c_j become very close (almost nearly zero), the output of the layer is almost equal to 1, and when passing through the second layer, the output value is almost equal to the weight value of the second layer. After such training, RBF NN was found to offer fast learning speed on the local network.

3.3. The Algorithm of RBF NN based on GA

Genetic algorithm is an adaptive and global probabilistic search algorithm, which simulates the criterion of survival of the fittest. The genetic algorithm mainly includes five basic steps: Coding, generating initial population, setting function of the fitness, designing the genetic operator, and determining the operating parameters. The process of GA is shown in Figure 6. The steps are as follows:

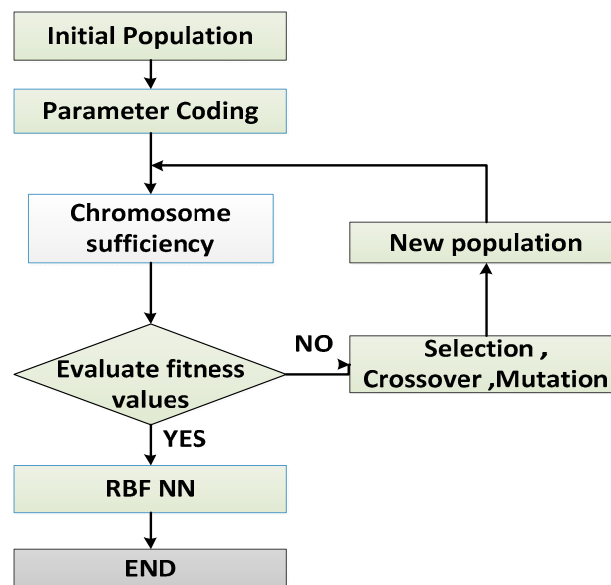


Figure 6. The process of RBF NN based on GA (RBF NN + GA).

(1) Random numbers are generated by a random number generator, which is set to the initial set of RBF NN. At the same time, the GA run parameters are set.

(2) Define the fitness function, judge the individual’s ability to adapt to the environment through the fitness function, and set the individual fitness value f .

(3) Evaluate the fitness value. If the fitness value $f < \delta$ (δ is the set error value), the requirement is met, training is stopped, and the output parameter is sent to the RBF NN. These parameters are optimal.

(4) If the fitness value $f \geq \delta$, the selection, intersection, and mutation operations are performed to generate a new individual, that is to say, the parameters are updated, and the fitness value is calculated again.

(5) It is judged as to whether the fitness value satisfies the condition. If it is not satisfied, step (4) is repeated, and if satisfied, the optimal solution is delivered.

3.4. RBF NN Based on GA with KF

The Kalman filtering algorithm can be divided into two information update processes: time update and measurement update process; these processes are recursive. The KF process is shown in Figure 7.

During the time update process, two updates are completed. Firstly, the state transition matrix is used to combine the $k - 1$ time information to complete the prediction of the value of k time. Secondly, the calculation of the one-step prediction mean square error is completed, and the quality of the prediction is quantitatively described. In summary, the transition from $k - 1$ to k is completed by using information related to system dynamics.

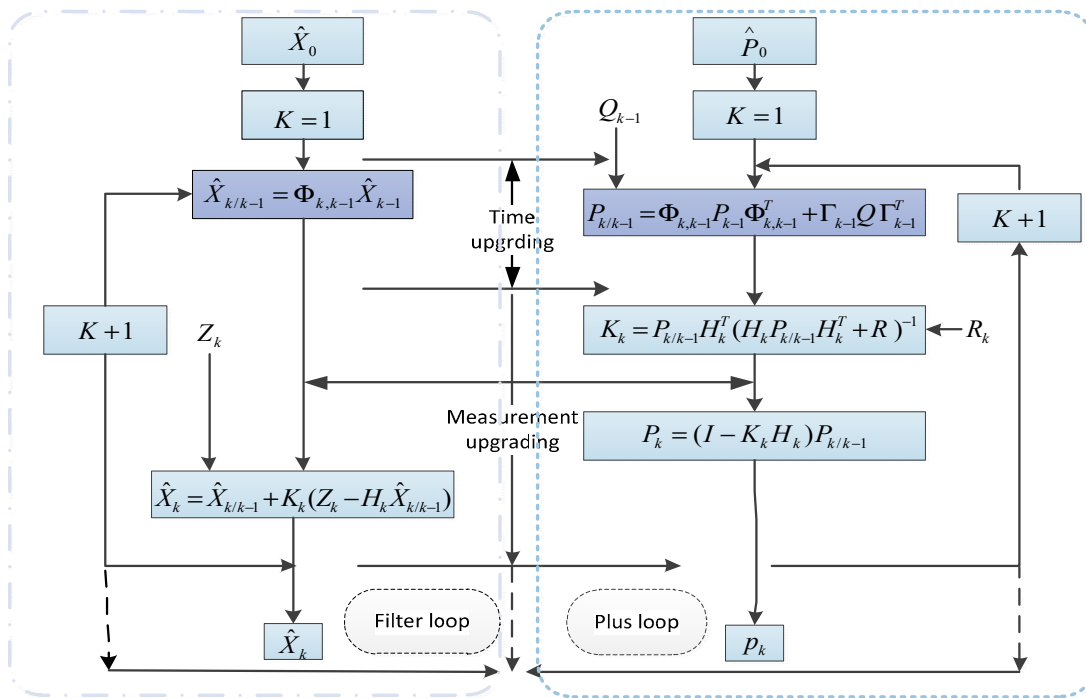


Figure 7. The Kalman filter (KF) process.

During the measurement update process, the remaining three formulas are utilized, which can make full use of the measured values and residuals. Finally, the optimal value of the estimator and the smaller estimation error is obtained.

One-step prediction of state:

$$\hat{X}_{k/k-1} = \Phi_{k,k-1} \hat{X}_{k-1} \tag{7}$$

State estimate:

$$\hat{X}_k = \hat{X}_{k/k-1} + K_k (Z_k - H_k \hat{X}_{k/k-1}) \tag{8}$$

Filter gain:

$$K_k = P_{k/k-1} H_k^T (H_k P_{k/k-1} H_k^T + R)^{-1} \tag{9}$$

One-step prediction of mean square error:

$$P_{k/k-1} = \Phi_{k,k-1} P_{k-1} \Phi_{k,k-1}^T + \Gamma_{k-1} Q \Gamma_{k-1}^T \tag{10}$$

Estimated mean square error:

$$P_k = (I - K_k H_k) P_{k/k-1} \tag{11}$$

where H_k is a measurement matrix, $P_{k/k-1}$ is a matrix of prior estimate error covariance; K_k is a filter gain matrix; P_k is a matrix of estimation error variance; R is the covariance of measurement noise covariance; Q is the covariance of process noise. According to the above formula, it can be found that if the initial value of \hat{X}_0 and P_0 are determined, the state estimation of $\hat{X}_k (k = 1, 2, \dots)$ at k moment can be calculated by the measurement vector of Z_k at k moment.

In this section, the three algorithms of KF, RBF NN and GA are merged, and the RBF NN + GA + KF fusion algorithm is established. The algorithm is online in real-time and also has certain learning abilities. Combined with the temperature drift model, the RBF NN + GA + KF temperature compensation model fusion algorithm is determined. The flow chart of the fusion algorithm is shown in Figure 8.

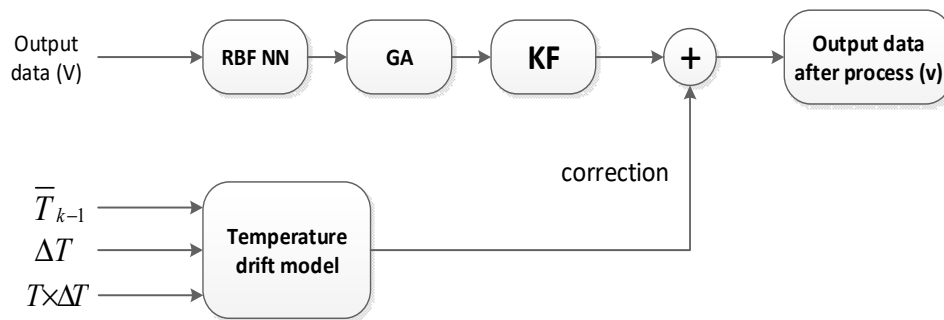


Figure 8. The process of RBF NN + GA + KF fusion algorithm.

The steps of RBF NN + GA + KF temperature compensation model fusion algorithm are as follows:

- (1) Initial (original) data is generated in the temperature experiment.
- (2) Using the neural network method to establish the temperature drift model, the temperature, temperature variation rate and temperature product term are taken as the input of the model.
- (3) The output data based on RBF NN + GA + KF is corrected by the output data of the temperature drift model, and then the temperature compensation model fusion algorithm is established.
- (4) Temperature compensation model fusion algorithm based on RBF NN + GA + KF is established as shown in Figure 8.
- (5) Output the data processed by the RBF NN + GA + KF temperature compensation model fusion algorithm.

4. Temperature Experiment Proposal

Through temperature experiments, the temperature characteristic of MEMS, the accelerometer, can be tested. In the temperature experiment, the temperature controlled oven can accurately provide a temperature range of $-50\text{ }^{\circ}\text{C}$ to $+150\text{ }^{\circ}\text{C}$. This ensures precise control of the accelerometer test temperature. The experimental equipment is shown in Figure 9. A power supply (GWINSTEK GPS-4303C, Good Will Instrument Co., Suzhou, Jiangsu, China) is employed to provide +5V voltage to HGMA, and a high-speed data acquisition system and a computer are employed to collect the HGMA output signal. The temperature is $25\text{ }^{\circ}\text{C}$ (room temperature value).

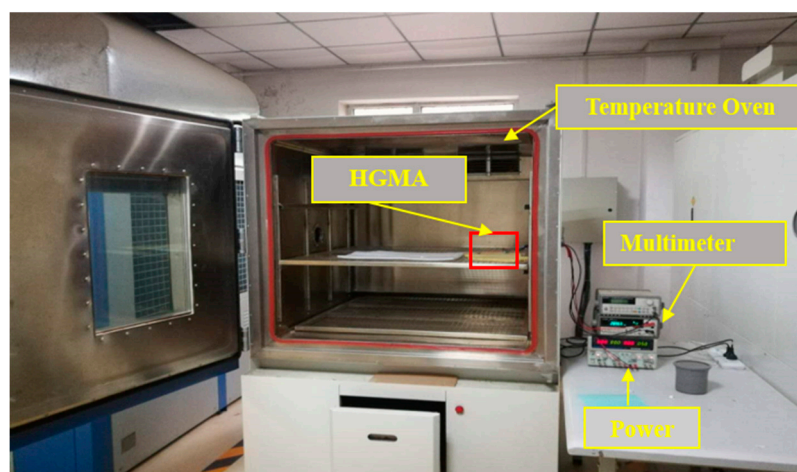


Figure 9. Temperature test equipment.

First, the oven temperature range is set between $-10\text{ }^{\circ}\text{C}$ and $60\text{ }^{\circ}\text{C}$. Then, power is switched on, and it starts to pick up data, which includes HGMA output and temperature value (a thermal resistance is arranged with HGMA to provide real temperature information). The data collection process is continuous (Figure 10).

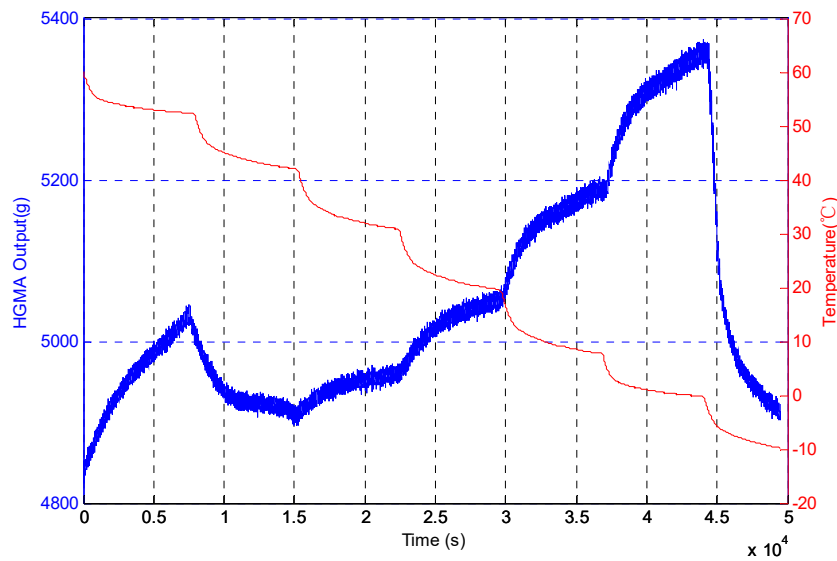


Figure 10. The output of MEMS in the temperature experiment.

5. Verification and Analysis

The experimental results of the MEMS accelerometer temperature experiment are shown in Figure 10. It can be seen that when the temperature changes from $-10\text{ }^{\circ}\text{C}$ to $60\text{ }^{\circ}\text{C}$, the acceleration output signal is approximately 5367 g . This means that the output of HGMA is greatly affected by temperature. To compensate for the accelerometer signal temperature, three temperature compensation models (RBF NN, RBF NN + GA, and RBF NN + GA + KF) are established here, as shown in Figure 11.

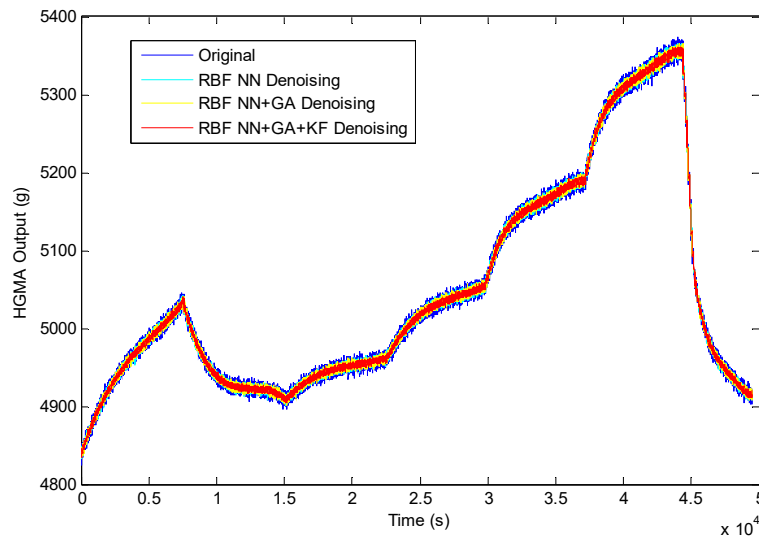


Figure 11. The three temperature energy models influence drift of the accelerometer.

Based on the established model, the results of the above models are calculated, as can be seen from Figure 11. All three models can approximate the original data very well, but RBF NN + GA + KF does a good job at suppressing noise. This work then employs the RBF NN + GA + KF denoising method and temperature drift method to improve HGMA precision. As can be seen from Figure 12, when the temperature changes from $-10\text{ }^{\circ}\text{C}$ to $60\text{ }^{\circ}\text{C}$, the acceleration output signal is approximately 385 g . This means that the fusion algorithm can effectively reduce the influence of temperature drift on HGMA precision.

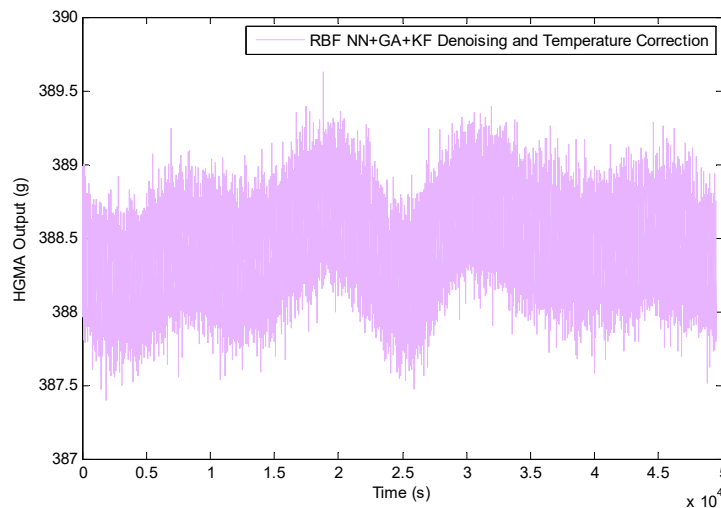


Figure 12. The compensation results of accelerometer based on three methods.

Allan variance is employed to evaluate the denoising and temperature compensation result of the methods; the results are shown in Figure 13. The acceleration random walking and bias stability (referring to angular random walking and bias stability of gyroscope) results of the original signal, RBF NN denoising, RBF NN + GA and RBF NN + GA + KF are 17130 g/h/Hz^{0.5}, 4720 g/h; 11470 g/h/Hz^{0.5}, 3595 g/h; 10760 g/h/Hz^{0.5}, 3416 g/h; 6918 g/h/Hz^{0.5}, 2587 g/h, respectively. And after temperature correction, the acceleration random walking and bias stability of HGMA during −10 °C to 60 °C are 765.3 g/h/Hz^{0.5} and 57.27 g/h. The results are shown in Table 3.

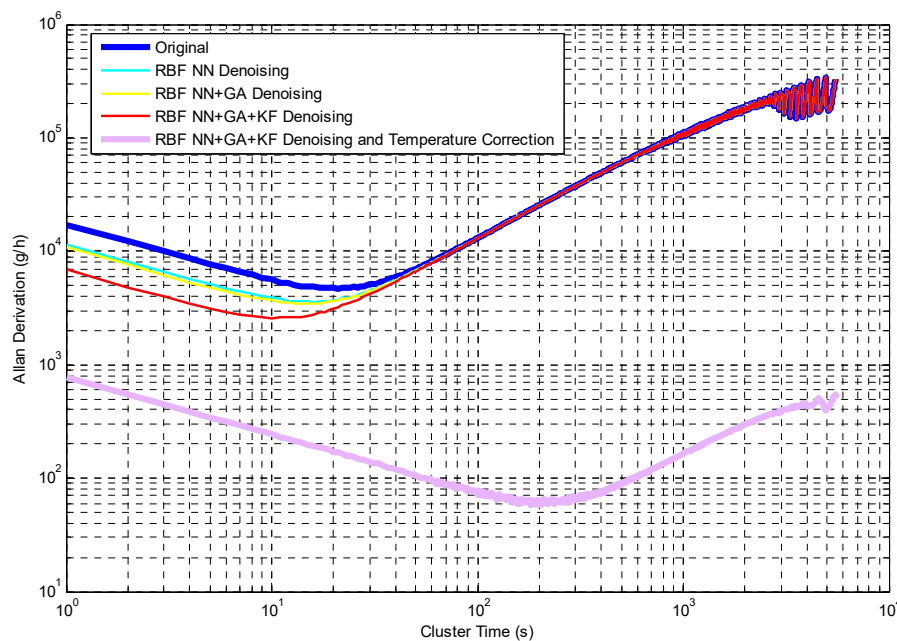


Figure 13. The Allan variance derivation of the compensation results of HGMA based on three methods.

Table 3. Results of Allan variance analysis.

De-Noising				Temperature Compensation			
Original data		RBF NN		RBF NN + GA		RBF NN + GA + KF	
B(g/h/Hz ^{0.5})	N(g/h)						
17130	4720	11470	3595	10760	3416	6918	2587
						765.3	57.27

6. Conclusions

This paper studies the design, fabrication, and corresponding algorithms to compensate for the temperature drift in a new HGMA. The accelerometer structure uses a beam structure. The simulation results show that the resonant frequency of HGMA in the 1st order mode is 408 kHz. The 2nd mode resonant frequency is 667kHz, and the gap with the first mode is 260 kHz, so the coupling movement between the two modes is small, and HGMA has better linearity. For the temperature compensation of HGMA, four algorithms are proposed: RBF NN, RBF NN + GA, RBF NN + GA + KF and the RBF NN + GA + KF method compensated by the temperature drift model. First, the temperature drift accuracy is improved by the RBF neural network. Second, GA is used to optimize the parameters of the RBF NN. Next, the Kalman filter algorithm is used to optimize the output value, and then the temperature drift model is used to compensate RBF NN + GA + KF. Finally, a new fusion algorithm of RBF NN + GA + KF combined with the temperature drift model is proposed. The fusion algorithm can effectively compensate the temperature drift of the HGMA. At last, the Allan variance coefficient shows a comparison of the three methods with the original data. The data shows that if the RBF NN + GA + KF method combined with the temperature drift model is used, acceleration random walking is from 17130 g/h/Hz^{0.5} to 765.3 g/h/Hz^{0.5}, and bias stability is from 4720 g/h to 57.27 g/h.

Author Contributions: H.C., L.P. and M.Z. conceived and designed the experiments; C.S. and Y.S. performed the experiments; J.L. and Z.X. analyzed the data, and M.Z. wrote the paper.

Funding: This work is supported by National Natural Science Foundation of China (No. 51705477, No. 61703098 and No.61603353), and Pre-Research Field Foundation of Equipment Development Department of China No.61405170104. The research is also supported by a program for the Top Young Academic Leaders of Higher Learning Institutions of Shanxi, Fund Program for the Scientific Activities of Selected Returned Overseas Professionals in Shanxi Province, Shanxi Province Science Foundation for Youths (No. 201801D221195), Young Academic Leaders of North University of China (No. QX201809), the Open Fund of State Key Laboratory of Deep Buried Target Damage No. DXMBJJ2017-15, and the Fund for Shanxi “1331 Project” Key Subjects Construction.

Conflicts of Interest: The authors declare no conflicts of interest.

References

- Ding, X.; Zhu, K.; Li, H. A Switch-bridge Based Readout Circuit for Differential Capacitance Measurement in MEMS Resonators. *IEEE Sens. J.* **2017**, *17*, 6978–6985. [[CrossRef](#)]
- Liu, Y.; Ma, T. Parasitic Resistance-Based High Precision Capacitive MEMS Accelerometer Phase Shift and Its Usage for Temperature Compensation. *IEEE Sens. J.* **2018**, *18*, 629–634. [[CrossRef](#)]
- Li, B.; Zhao, Y.; Li, C.; Cheng, R.; Sun, D.; Wang, S. A Differential Resonant Accelerometer with Low Cross-Interference and Temperature Drift. *Sensors* **2017**, *17*, 178. [[CrossRef](#)] [[PubMed](#)]
- Tsai, M.H.; Liu, Y.C.; Liang, K.C.; Fang, W. Monolithic CMOS–MEMS Pure Oxide Tri-Axis Accelerometers for Temperature Stabilization and Performance Enhancement. *J. Microelectromech. Syst.* **2015**, *24*, 1916–1927. [[CrossRef](#)]
- Xu, Y.; Ahn, C.K.; Shmaliy, Y.S.; Chen, X.; Li, Y. Adaptive robust INS/UWB integrated pedestrian tracking using UFIR filter bank. *Measurement* **2018**, *123*. [[CrossRef](#)]
- Yang, B.; Dai, B.; Liu, X.; Xu, L.; Deng, Y.; Wang, X. The on-chip temperature compensation and temperature control research for the silicon micro-gyroscope. *Microsyst. Technol.* **2015**, *21*, 1061–1072. [[CrossRef](#)]
- Cao, H.; Li, H.; Liu, J. An improved interface and noise analysis of a turning fork microgyroscope structure. *Mech. Syst. Signal Process.* **2016**, *70–71*, 1209–1220. [[CrossRef](#)]
- Cao, H.; Li, H.; Shao, X.; Liu, Z.; Kou, Z.; Shan, Y.; Shi, Y.; Shen, C.; Liu, J. Sensing mode coupling analysis for dual-mass MEMS gyroscope and bandwidth expansion within wide-temperature range. *Mech. Syst. Signal Process.* **2018**, *98*, 448–464. [[CrossRef](#)]
- Cao, H.; Zhang, Y.; Han, Z.; Shao, X.; Gao, J.; Huang, K.; Shi, Y.; Tang, J.; Shen, C.; Liu, J. Pole-Zero-Temperature Compensation Circuit Design and Experiment for Dual-mass MEMS Gyroscope Bandwidth Expansion. *IEEE/ASME Trans. Mechatron.* **2019**. [[CrossRef](#)]

10. Cao, H.; Li, H.; Sheng, X.; Wang, S.; Yang, B.; Huang, L. A novel temperature compensation method for MEMS gyroscope's oriented on periphery circuit. *Int. J. Adv. Robot. Syst.* **2013**, *10*. [[CrossRef](#)]
11. Lee, J.; Rhim, J. Temperature compensation method for the resonant frequency of a differential vibrating accelerometer using electrostatic stiffness control. *J. Micromech. Microeng.* **2012**, *22*, 095016. [[CrossRef](#)]
12. Li, D.; Li, X. Quartz Flexible Accelerometer Temperature Characteristic and Scale Factor. *Ferroelectrics* **2013**, *457*, 6.
13. Dominik, J. Three axial low temperature cofired ceramic accelerometer. *Microelectron. Int.* **2013**, *30*, 125–133.
14. Yang, W.; Fang, B.; Tang, Y.; Qin, X. A Temperature Compensation Model for Low Cost Quartz Accelerometers and Its Application in Tilt Sensing. *Math. Probl. Eng.* **2016**, *2016*, 2950376. [[CrossRef](#)]
15. He, J.; Xie, J.; He, X.; Du, L.; Zhou, W. Analytical study and compensation for temperature drifts of a bulk silicon MEMS capacitive accelerometer. *Sens. Actuators A Phys.* **2016**, *239*, 174–184. [[CrossRef](#)]
16. Cao, Q.; Zhong, M. An adaptive strong tracking Kalman filter for position and orientation system. *Trans. Inst. Meas. Control* **2016**, *38*, 1212–1224. [[CrossRef](#)]
17. Ruzza, G.; Guerriero, L.; Revellino, P.; Guadagno, F.M. Thermal Compensation of Low-Cost MEMS Accelerometers for Tilt Measurements. *Sensors* **2018**, *18*, 2536. [[CrossRef](#)]
18. Shen, C.; Yang, J.; Tang, J.; Liu, J.; Cao, H. Note: Parallel processing algorithm of temperature and noise error for micro-electro-mechanical system gyroscope based on variational mode decomposition and augmented nonlinear differentiator. *Rev. Sci. Instrum.* **2018**, *89*, 076107. [[CrossRef](#)]
19. Zhang, J.; Wang, Y.; Zega, V.; Su, Y.; Corigliano, A. Nonlinear dynamics under varying temperature conditions of the resonating beams of a differential resonant accelerometer. *J. Micromech. Microeng.* **2018**, *28*, 075004. [[CrossRef](#)]
20. Cheng, J.; Qi, B.; Chen, D.; Landry, R., Jr. Modification of an RBF ANN-based temperature compensation model of interferometric fiber optical gyroscopes. *Sensors* **2015**, *15*, 11189–11207. [[CrossRef](#)]
21. Huang, H.; Chen, X.; Zhang, B.; Wang, J. High accuracy navigation information estimation for inertial system using the multi-model EKF fusing adams explicit formula applied to underwater gliders. *ISA Trans.* **2017**, *66*, 414–424. [[CrossRef](#)] [[PubMed](#)]
22. Xu, Y.; Tian, G.; Chen, X. Enhancing INS/UWB integrated position estimation using federated EFIR filtering. *IEEE Access* **2018**, *6*, 64461–64469. [[CrossRef](#)]
23. Shen, C.; Song, R.; Li, J.; Zhang, X.; Tang, J.; Shi, Y.; Liu, J.; Cao, H. Temperature drift modeling of MEMS gyroscope based on genetic-Elman neural network. *Mech. Syst. Signal Process.* **2016**, *72–73*, 897–905.
24. Xia, D.; Kong, L.; Hu, Y.; Ni, P. Silicon microgyroscope temperature prediction and control system based on BP neural network and Fuzzy-PID control method. *Meas. Sci. Technol.* **2015**, *26*, 2. [[CrossRef](#)]
25. Cao, H.; Zhang, Y.; Shen, C.; Liu, Y.; Wang, X. Temperature Energy Influence Compensation for MEMS Vibration Gyroscope Based on RBF NN-GA-KF Method. *Shock Vib.* **2018**, *2018*, 2830686. [[CrossRef](#)]
26. Shi, Y.; Yang, Z.; Ma, Z.; Cao, H.; Kou, Z.; Zhi, D.; Chen, Y.; Feng, H.; Liu, J. The development of a dual-warhead impact system for dynamic linearity measurement of a high-g micro-electro-machanical-system (MEMS) accelerometers. *Sensors* **2016**, *16*, 840. [[CrossRef](#)] [[PubMed](#)]
27. Shi, Y.; Zhao, Y.; Feng, H.; Cao, H.; Tang, J.; Li, J.; Zhao, R.; Liu, J. Design, Fabrication and Calibration of a High-G MEMS Accelerometer. *Sens. Actuators A Phys.* **2018**, *279*, 733–742. [[CrossRef](#)]

